Research Article | Vol. 27, No. 16 | 5 Aug 2019 | OPTICS EXPRESS 22352
Optics EXPRESS

# 3D microphotonic probe for high resolution deep tissue imaging

MOHAMMAD AMIN TADAYON,[1,2] SHRIDDHA CHAITANYA,[1] KELLY MARIE MARTYNIUK,[3] JOSEPHINE CECELIA MCGOWAN,[3] SAMANTHA PAMELA ROBERTS,[1] CHRISTINE ANN DENNY,[3] AND MICHAL LIPSON[1,*]

[1]*Department of Electrical Engineering, Columbia University, New York, NY, USA*
[2]*Lensguide Imaging Technology, Inc., Gaithersburg, MD, USA*
[3]*Department of Psychiatry, Columbia University, New York, NY, USA*
** ml3745@columbia.edu*

**Abstract:** Ultra-compact miniaturized optical components for microendoscopic tools and miniaturized microscopes are required for minimally invasive imaging. Current microendoscopic technologies used for deep tissue imaging procedures are limited to a large diameter and/or low resolution due to manufacturing restrictions. We demonstrate a platform for miniaturization of an optical imaging system for microendoscopic applications with a resolution of 1 µm. We designed our probe using cascaded micro-lenses and waveguides (lensguide) to achieve a probe as small as 100 µm x 100 µm with a field of view of 60 µm in diameter. We demonstrate wide-field microscopy based on our polymeric probe fabricated using photolithography and a two-photon polymerization process.



## 1. Introduction

High resolution miniaturized microendoscopic tools used for deep tissue imaging are vital for medical diagnosis and treatment. Miniaturization of these tools results in minimal tissue damage during the imaging process. Current endoscopic technologies used for deep tissue imaging are of large size or low resolution due to manufacturing restrictions. For example, fiber optic bundle technology [1,2] used for confocal imaging [3], multi-photon imaging [4], and calcium imaging [5] is constrained in resolution by the size of the individual fiber in the fiber optic bundle [6]. Miniaturized lenses [2–7] used for confocal imaging [3] and endo-microscopes [2] are constrained in size to millimeter scale by the manufacturing process based on grinding and polishing [8]. GRIN lenses with a diameter of 0.5-1 mm are used for brain tissue imaging with single [9–12] or two-photon [11–14] imaging techniques as well as for optical coherence tomography imaging of the esophagus [15] and coronary artery [16]. These lenses have enabled the study of deep brain areas [9] including the hypothalamic network for appetitive behaviors [17] and hippocampal CA1 for memory encoding [18]. However, GRIN lenses suffer from a tradeoff between the size of the cross sectional area and resolution because of the technological challenge of being able to form a strong refractive index gradient [19] within a small cross sectional area. This restriction results in GRIN lenses used for deep tissue imaging with large cross-sectional dimensions between 0.5 mm and 1 mm in diameter. Next-stage microendoscopic imaging tools must be smaller and have a higher resolution to enable more advanced tissue imaging and analysis for medical imaging.

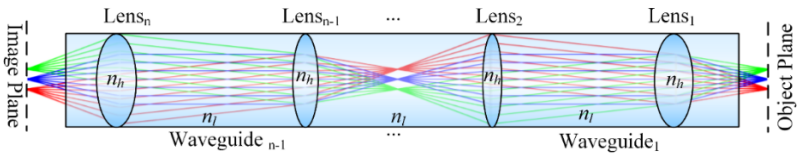


Fig. 1. Schematic of the lensguide platform.

#366648 https://doi.org/10.1364/OE.27.022352
Journal © 2019 Received 24 May 2019; revised 6 Jul 2019; accepted 10 Jul 2019; published 23 Jul 2019

Optics EXPRESS

We present a platform for miniaturizing an optical imaging column for endoscopic applications that achieves a diffraction limited imaging resolution. We use cascaded polymeric micro-lenses and waveguides (lensguides) to achieve a higher resolution and larger field of view compared to the current single micro-lens on the tip of a waveguide [20]. In contrast to GRIN lenses that use a gradient index profile, our lensguide probe is based on the shape and refractive index of each of the lenses, allowing us to fabricate a probe of arbitrary size and numerical aperture without the index gradient profile restriction of the GRIN lens. We use multiple lenses and waveguides to capture an image and guide it through the cascaded lenses and waveguides (Fig. 1). By using multiple lenses, we redirect the diffracted light ensuring that light is located at the center of the waveguide and not reflected at its interface, a design that eliminates the formation of multiple images. In addition to the miniaturization of the probe, our platform enables the increase of the probe length by adding more lenses, resulting in a long probe for very deep tissue imaging.

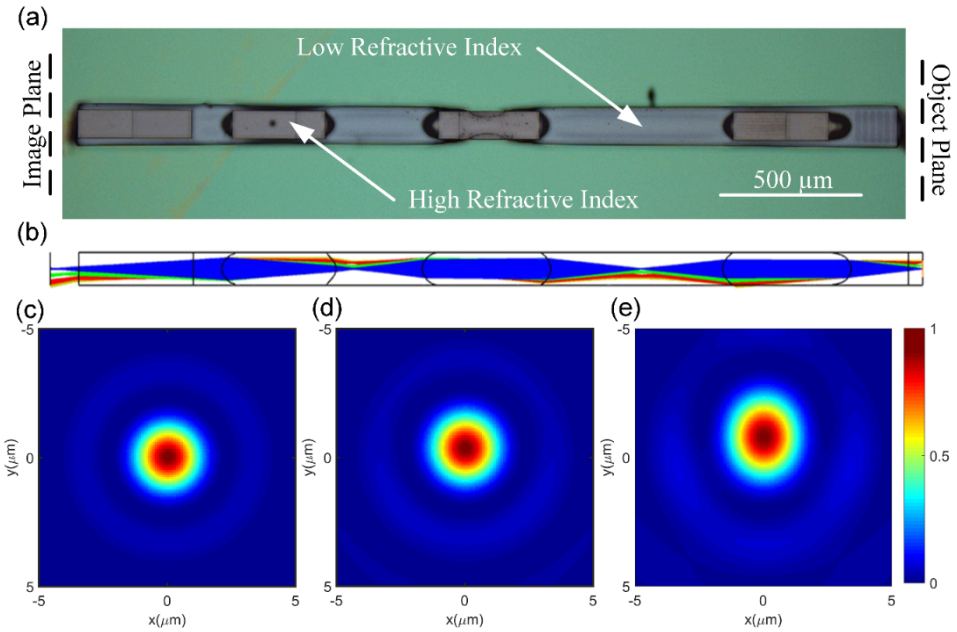


Fig. 2. (a) Fabricated lensguide. The higher refractive index is IP-S and the lower refractive index is NOA 1348. (b) Design and light beam propagation along the probe of 100 µm x 100 µm cross section and about 3 mm length. (c-e) the simulated point spread function for the point source located on the optical axis, 10 µm above the optical axis, and 20 µm above the optical axis in the object plane respectively.

## 2. Methods

We control aberration using an aspheric lens profile and by introducing additional surfaces. We also use aspheric surfaces to bring the focal plane closer to the lens to achieve a higher numerical aperture than spherical lenses using the same combination of material. We use Nanoscribe IP-S (Nanoscribe GmbH) as the higher index material and NOA 1348 (Norland Products) as the lower index material. In this design, the image object is immersed in 50 µm of water from the probe front-end, and the final image is located in air 100 µm away from the probe back-end. We optimize the profile of each surface along the light path for different point sources located across the field of view (Figs. 2(a) and 2(b)). The major sources of aberrations are the spherical and the coma. Figures 2(c)-2(e) shows the minimal variation of the point spread function across the field of view as a result of the optimization of each surface along the light path. We compare this design with the design where the lens profiles

Optics EXPRESS

are not optimized along the light path and observe the degradation of the point spread function across the field of view (Figs. 6(b)-6(d)). Note that the use of the same lens profile along the light path for all lenses leads to a design similar to the design of conventional GRIN lenses. Additional discussion of our lensguide design and the selection of surfaces can be found in Appendix 1 and 2.

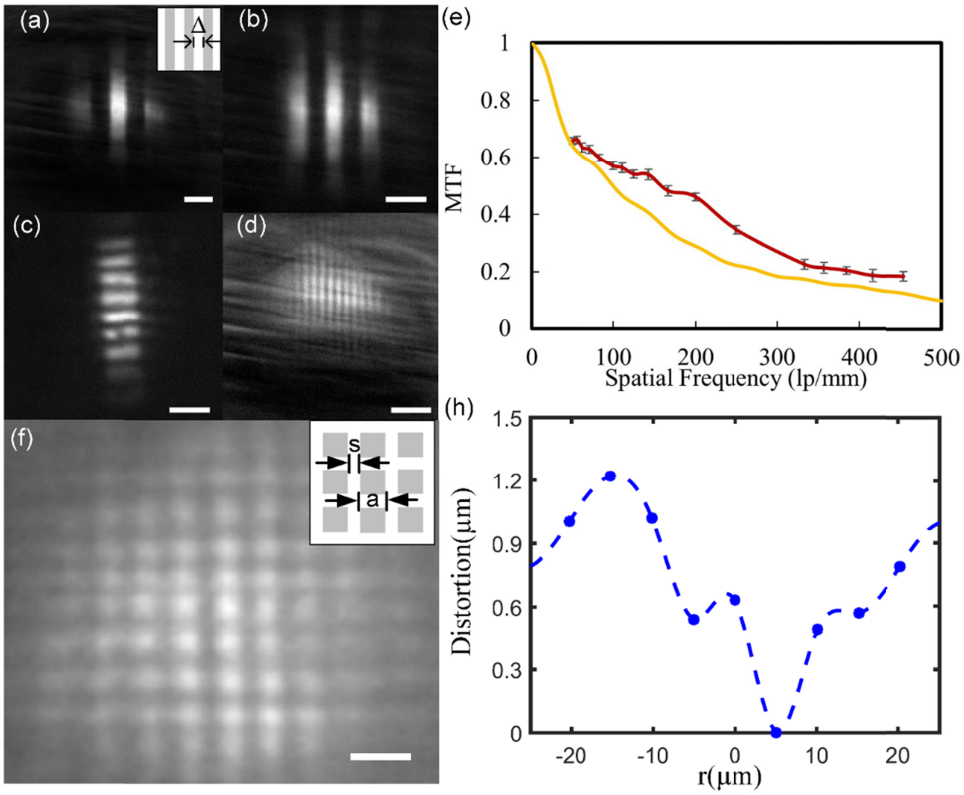


Fig. 3. Imaging of a grid line target with spacing of (a) Δ = 7 μm. (b) Δ = 4.5 μm, (c) Δ = 2 μm, and (d) Δ = 1.2 μm through the lensguide. Inset in (a) shows the schematic of the imaging target, (e) Probe modulation transfer function based on the measurement (red) and on the OpticStudio simulation (yellow). (f) Image of a distortion grid target with a = 3 μm and s = 2 μm. Inset shows the schematic of the imaging target. (h) Distortion across the whole field of view. The dots are the measured data. The line is a guide for the eye. All scale bars are 10 um.

We fabricate our polymeric lensguide probe based on two-photon polymerization and photolithography. To fabricate the lenses, we use a two-photon polymerization 3D printer (Photonic Professional GT from Nanoscribe GmbH). Using our 3D CAD file, the machine exposes the lens polymer with the higher refractive index (e.g. IP-S from Nanoscribe GmbH) [21–24]. After fabrication of the cascade of micro-lenses, the areas between the lenses are filled with a lower index polymer (NOA 1348 from Norland Products). The cascade of micro-lenses is capped with a mask with a waveguide pattern. To avoid the lower index polymer from sticking to the waveguide mask after exposure, the mask is treated in fluoroctatrichlorosilane (FOTS) vapor. We align the waveguide mask and the cascade of micro-lenses and use a holder to hold them together. Using capillary forces, we then flow the lower index polymer (with low viscosity) into the gap between the waveguide mask and the substrate. Finally, we expose the low refractive index polymer from the mask side and the waveguide mask is released. Figure 2(a) shows the microscopic image of our fabricated device.

Optics EXPRESS

## 3. Results

We demonstrate that our probe design is able to resolve lithographic features as small as 1 μm consistent with our theoretical design in the Optics Studio (Zemax). To determine the resolution of the probe, we image a target consisting of lithographically defined metallic grid lines spaced by Δ varying between 1 μm and 10 μm through a fabricated probe. The metallic lines on the grid are defined using electron beam lithographic patterning of an aluminum/chrome film deposited on a fused silica substrate. In Figs. 3(a)-3(d) we show some of the images of different resolution targets through the lensguide. The probe used is 100 μm x 100 μm in cross section and 3 mm long. The entire probe structure is fabricated using two polymers with refractive indices of 1.520 and 1.348. We image the target by illuminating it via the probe and then projecting its image on a scientific CMOS camera using a 50x objective with an NA of 0.55. We subtract the background image from our captured images. The strength of the signal from this background image depends on the distance between the last surface of the lensguide and the image plane, the amount of reflection from the last surface, the illumination method, and the lensguide background reflection and autofluorescence. Engineering of these parameters minimizes the strength of the background image [20]. The working distance between the object and the lens is approximately 100 μm. We show in Figs. 3(a)-3(e) that the probe is able to resolve features spaced by about 1 μm. Additional details about the imaging setup are described in Appendix 4.

To evaluate the performance of our imaging probe for different spatial frequencies, we measure the modulation transfer function (MTF) using a resolution target with a resolution between 50 to 450 lp/mm. Our experimental results are in good agreement with our OpticStudio simulation (Fig. 3(e)). Like other lens systems as well as GRIN lenses, the magnification, resolution, and field of view of our lensguide varies depending on the distance of the object from the probe. We measure the MTF in the air for an object located 50 μm from the tip of the probe. The magnification of the probe is approximately 2 and the field of view is 60 μm. With a slight decrease in resolution we are able to increase the field of view to 100 μm. In Visualization 1, we show the quality of the imaging probe based on the modification of each surface; in Visualization 2, we show the repetition of the same profile along the light path. For additional comparison with the expected performance based on our simulations we also show the images of the test target and measured MTF (Fig. 3).

We observe minimal distortion level across the whole field of view by imaging a grid distortion target (Fig. 3(f)) through the lensguide. In Fig. 3(h), we show a maximum of 1.2 μm distortion across 50 μm diameter of imaging space. The grid distortion target consists of 3 μm squares with 2 μm spacing. We calculate the probe distortion by measuring the variation of the distance between the peaks of each period in the image plane.

As an example of an application of our microendoscopic platform for fluorescence imaging, we image micro-beads as well as brain slices using wide-field microscopy via our fabricated probe. Figure 4(a) shows the imaging of 6 μm fluorescent beads (with peak emission at 520 nm) through the probe with a high signal to noise ratio of 250 (Fig. 4(b)). As an example of an application of our platform for tissue imaging, we show an image of the dentate gyrus region of the brain by imaging activated neural cells in brain slices using wide-field microscopy via our fabricated probe (Fig. 4(c)). Wide field microscopy has been utilized for imaging neural activities in different brain regions [25,26]. Unlike two-photon microscopy, in wide-field microscopy all pixels in an image are recorded simultaneously. For high speed functional imaging, this method is advantageous over two-photon microscopy. The slices in our example are from an ArcCreERT2 [27] x channelrhodopsin (ChR2)-enhanced yellow fluorescent protein (EYFP) [28] transgenic mouse. This mouse line offers permanent membrane bound EYFP labeling of Arc + neurons activated during the learning experience [27]. Additional details on preparation of the slices are described in Appendix 5. The quality of our brain slice images is comparable with our table top wide-field imaging system. A higher imaging quality image is expected using a controlled environment for a

Optics EXPRESS

brain slice. Our probe can be inserted into the brain for in vivo imaging. Additional information on the insertion of these probes in the animal brain can be found in [20], and [29–31].

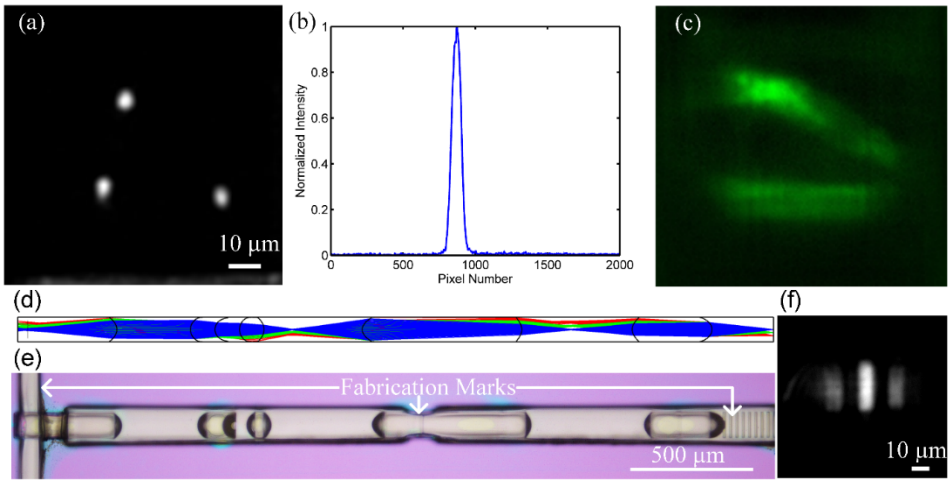


Fig. 4. (a) Image of 6 µm microbeads. (b) Intensity signal profile from the 6 µm bead. (c) Image of the dentate gyrus. (d) Design of the probe with a different polymer. (e) Image of the fabricated device. (f) Image of the 6 µm imaging target in front of the probe.

In the fabrication process, we show the use of different polymers with different refractive indices and dispersion properties to achieve a variety of optical properties as well as to enable chromatic aberration correction. We design and fabricate a lensguide with the same size using the combination of OrmoComp (microresist technology) and NOA 1348 (Norland Products). The OrmoComp has a refractive index of 1.520 and NOA 1348 has a refractive index of 1.348. Figure 4(d) shows the design of the probe with magnification of 1 in the OpticStudio. The fabrication process is similar to the fabrication of our lensguide using IP-S (used for imaging in Fig. 3) and NOA 1348. Figure 4(e) shows an image of the fabricated probe, where we replace the IP-S with OrmoComp. While OrmoComp requires a higher exposure dosage for the 2 photon polymerization than IP-S, the amount of auto-fluorescence in OrmoComp is significantly lower than for IP-S, a feature that can be helpful for reducing background noise in the image. Figure 4(f) shows an image of the 6 µm imaging target located in front of the device. Additional discussion on the effect of autofluorescence can be found in [20].

## 4. Conclusion

In summary, our lensguide allows for a completely new generation of miniaturized endoscopy probes to be utilized for a variety of optical imaging techniques. In contrast to the GRIN lenses used today, our lensguide results in minimal damage to imaged tissue. Using polymers with a refractive index between 1.3 and 1.7 lensguide achieves a wide range of numerical apertures and guiding properties. In neuroscience applications, for example, our miniaturized probe can be used in applications such as wide field microscopy and multi-photon imaging for imaging and excitation of deep layers of the brain. In medical imaging applications, our imaging probe could enable new applications that require sub-cellular resolution for diagnostics involving multimodality techniques such as fluorescence imaging (auto-fluorescence or via an injected dye), and optical coherence tomography. These techniques are currently being introduced using endoscopic instruments that are several mm wide resulting in significant amount of damage to tissue. The miniature size of our lensguide, however, could replace current endoscopic instruments and result in minimal tissue damage during imaging procedures. Utilizing different types of imaging techniques, our lensguide can be

Optics EXPRESS

used for identification of cancer tumor margins in cancer removal. Our imaging probe can be fabricated as a forward looking imaging probe as well as a side looking probe for endoscopes [20].

## Appendix

### *Appendix 1- Periodic imaging system with diffraction limited elements*

Here we discuss basic methods of our lensguide design. We show that correction of the aberration along the light path in the lensguide is necessary to prevent degradation of image quality. Because Repetition of the same period along the light path is unavoidable in conventional GRIN lenses we first consider repetition of the ideal imaging system (each period of the lensguide) and find the theoretical limit for this type of periodic structure. We show that repetition of the same type of period (with the same profile) along the light path leads to a reduction in resolution even if the designed period is the ideal imaging system with no aberration.

We can consider a period of the periodic imaging system as an imaging system with incoherent illumination which obeys intensity convolution between image intensity ($I_i$) and object intensity ($I_o$) [32],

$$I_i(u,v) = \iint_{-\infty}^{+\infty} \left|h(u-\tilde{\xi}, v-\tilde{\eta})\right|^2 I_o(\tilde{\xi},\tilde{\eta})\, d\tilde{\xi} d\tilde{\eta}, \tag{1}$$

$|h|^2$ is the intensity impulse response, $\tilde{\xi},\tilde{\eta}$, are the object plane coordinates multiplied with image magnification, and u, v are the image plane coordinates. The normalized frequency spectra of the object ($G_o$) and image ($G_i$) can be defined by [32]

$$\begin{aligned} G_o(f_x,f_y) &= \frac{\iint_{-\infty}^{+\infty} I_o(u,v)\exp[-j2\pi(f_x u + f_y v]\, du dv}{\iint_{-\infty}^{+\infty} I_o(u,v)\, du dv}, \\ G_i(f_x,f_y) &= \frac{\iint_{-\infty}^{+\infty} I_i(u,v)\exp[-j2\pi(f_x u + f_y v]\, du dv}{\iint_{-\infty}^{+\infty} I_i(u,v)\, du dv}, \end{aligned} \tag{2}$$

where $f_x = x/\lambda z_i$, and $f_y = y/\lambda z_i$, and x, and y are coordinates at the pupil. The normalized transfer function ( $\mathcal{H}$ ) can be written as [32]:

$$\mathcal{H}(f_x,f_y) = \frac{\iint_{-\infty}^{+\infty} \left|h(u,v)\right|^2 \exp[-j2\pi(f_x u + f_y v]\, du dv}{\iint_{-\infty}^{+\infty} \left|h(u,v)\right|^2\, du dv}, \tag{3}$$

Application of the convolution theorem to (1) yields the frequency domain relation [32],

$$G_i(f_x,f_y) = \mathcal{H}(f_x,f_y) G_o(f_x,f_y), \tag{4}$$

If our system is a periodic imaging system with *n* repetition of the same period, the image and object spectra can be related using

$$G_i(f_x,f_y) = \mathcal{H}(f_x,f_y)^n G_o(f_x,f_y). \tag{5}$$

Since $|\mathcal{H}(f_x f_y)| \leq 1$ [32], increasing the number of periods (number of images in the light path) would decrease the OTF value resulting in a decrease of the MTF value or imaging contrast. Figure 5 shows the MTF value for a periodic imaging structure with different repetition numbers. We can observe a decrease in the image contrast by increasing the number of

Optics EXPRESS

periods. We consider an aberration free (diffraction limited) imaging system for each of the periods. The aberration free circular pupil optical transfer function can be written as [32]:

$$\mathcal{H}(\rho)=\begin{cases}\dfrac{2}{\pi}\left[\arccos\left(\dfrac{f}{2f_{cut}}\right)-\dfrac{f}{2f_{cut}}\sqrt{1-\left(\dfrac{f}{2f_{cut}}\right)^{2}}\right] & f\le f_{cut}\\ 0 & otherwise\end{cases}, \tag{6}$$

$f_{cut} = w/\lambda z_i$, is the cutoff frequency of the coherent system. We can prevent the decrease in imaging contrast by engineering the walls of the waveguides (to decrease the number of periods) and gradually increasing the aperture size along the light path.

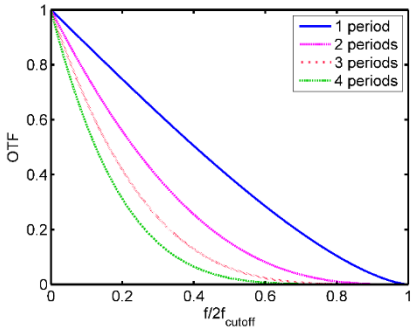


Fig. 5. In the periodic imaging System consisting of the diffraction limited periods, The OTF degrades with increase of number of periods.

### *Appendix 2- Effect of the aberration correction along the light path*

The effect of aberration can be considered by applying the generalized pupil function [32]:

$$P_i(x,y)=P_i(x,y)\exp[jkW_i(x,y)], \tag{7}$$

where $W_i(x,y)$ presents phase error at the point (x,y) of the pupil, and the $P_i(x,y)$ presents pupil function. The OTF of the i'th step with aberrations is written as [32]:

$$\mathcal{H}_i(f_x,f_y)=\frac{\iint_{A_i(f_x,f_y)} e^{jk\left[W_i\left(x_i+\frac{\lambda z_i f_x}{2},y_i+\frac{\lambda z_i f_y}{2}\right)-W\left(x_i-\frac{\lambda z_i f_x}{2},y_i-\frac{\lambda z_i f_y}{2}\right)\right]}dx_i dy_i}{\iint_{A_i(0,0)}dxdy}, \tag{8}$$

where $A_i(f_x,f_y)$ gives the overlap of the apertures in the i'th step. Considering $\mathcal{H}_i(f_x,f_y) = a_i(f_x,f_y)\exp(jW_i(f_x,f_y))$, we can write the whole system OTF as,

$$\mathcal{H}(f_x,f_y)=\prod_{i=1}^{n}\mathcal{H}_i(f_x,f_y)=\prod_{i=1}^{n}a_i(f_x,f_y)\exp\left(jW_i(f_x,f_y)\right). \tag{9}$$

We rewrite the above equation as,

$$\mathcal{H}(f_x,f_y)=\exp\left(j\sum_{i=1}^{n}W_i(f_x,f_y)\right)\prod_{i=1}^{n}a_i(f_x,f_y). \tag{10}$$

For the system with repetition of the same period, this equation is simplified to,

$$\mathcal{H}(f_x,f_y)=\exp\left(jnW_1(f_x,f_y)\right)a_1(f_x,f_y)^n. \tag{11}$$

Optics EXPRESS

However, by control of the aberration along the light path, we can find a system with the following condition,

$$\prod_{i=1}^{n} a_i\left(\mathrm{f_x},\mathrm{f_y}\right) \geq a_1\left(\mathrm{f_x},\mathrm{f_y}\right)^n ; \sum_{i=1}^{n} W_i\left(f_x,f_y\right) \leq nW_1\left(f_x,f_y\right). \tag{12}$$

The periodic imaging system with the condition above provides a higher performance than the repeating period system.

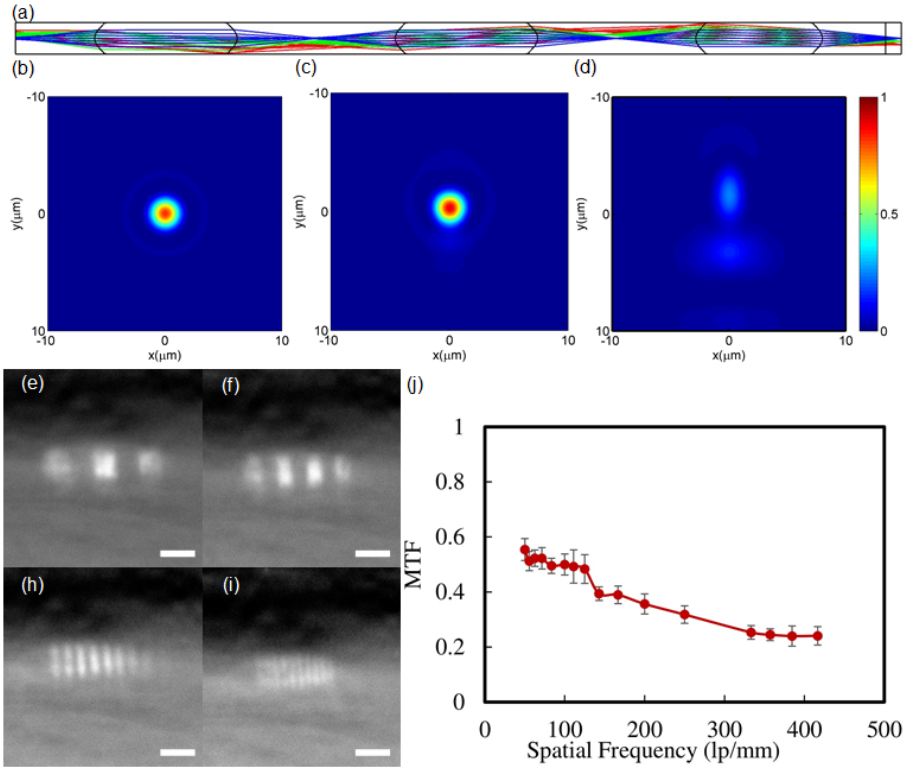


Fig. 6. (a) Design and the light beam propagation inside the probe (with repetition of the same periods) of 100 μm x 100 μm cross section and about 3 mm length. (b-d) the simulated point spread function for the point source located at 0 μm, 10 μm, and 20 μm respectively. Imaging of the resolution target of size of (e) 7 μm, (f) 4.5 μm, (h) 2 μm, and (i) 1.2 through the lensguide. (j) Measured probe modulation transfer function.

### *Appendix 3- Experimental results for the periodic lensguide without aberration correction along the light path*

To better understand the advantage of the aberration correction along the light path, we design and fabricate a probe without correcting for aberration along the light path (Fig. 6(a)). This probe is similar to multi period GRIN lenses since we do not change the surface profiles along the light path. Figure 6(b)-6(d) show the degradation of image quality (point spread function) across the field of view. Comparing Figs. 6(e)-6(i) and Figs. 4(a)-4(d), we observe a significant degradation of image quality in the constant profile imaging probe. Figure 6(j) shows the MTF of the constant profile imaging probe. We compare the quality of the imaging probe based on the modified profile (see Visualization 1) and the constant profile (see Visualization 2).

Optics EXPRESS

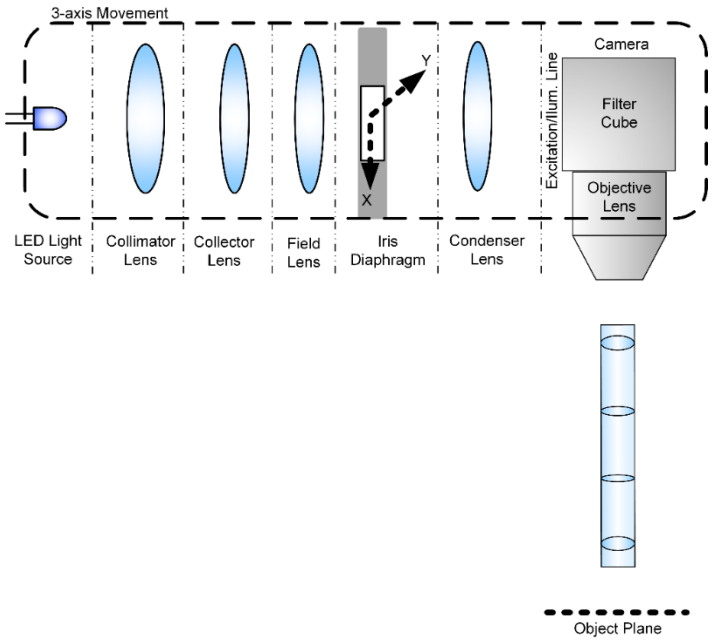


Fig. 7. Imaging setup to image through the lensguide.

### *Appendix 4- Imaging setup*

We use the imaging setup shown in Fig. 7 to characterize the imaging properties of our fabricated probe. We utilize the free space imaging setup located behind the lensguide to illuminate the object and then reconstruct the image formed at the backend of the lensguide. Our imaging setup can be replaced with any bright field microscopy system. We use the Köhler illumination method for the illumination. The image of the iris diaphragm is formed on the image plane of the imaging setup. We use the iris to make the illuminating area as small as the backend of the lensguide. For all of our imaging, we utilize a 50× objective with an NA of 0.55 (Mitutoyo M Plan Apo 50×) and a monochromatic Scientific CMOS camera (ORCA flash 4.0 LT Hamamatsu Photonics).

### *Appendix 5- eYFP transgenic mouse slice preparation*

To drive the expression of reporter enhanced yellow fluorescent protein (eYFP) in active neurons, 8-week-old ArcCreER$^{T2}$xChR2-eYFP mice received an intraperitoneal injection 4-hydroxytamoxifen. Five days later, the mice underwent a transcranial perfusion with ice-cold 1X phosphate-buffed saline (PBS) immediately followed by 4% paraformaldehyde (PFA). The brains were then quickly removed and submerged overnight in 4% PFA at 4°C. The following day, the brains were transferred to 1X PBS and 100 µm thick coronal tissue sections were cut using a vibratome (VT1200, Leica Biosystems). Free-floating brain slices were kept in 1X PBS with 0.01% sodium azide prior to the imaging of eYFP$^{+}$ neurons in the cerebral cortex with the probe.

## Funding

Columbia University Office of the Executive Vice President Research Initiatives in Science & Engineering (RISE).

## Acknowledgments

This work was performed in part at the Advanced Science Research Center (ASRC) at the Graduate Center of the City University of New York. M.A. Tadayon thanks D. Peterka, Y.-C.

Optics EXPRESS

Chang, N. Accanto, J.L. Kayfetz, and O.A.J. Gordillo for their helpful discussions, and feedback.

## References


1. B. A. Flusberg, E. D. Cocker, W. Piyawattanametha, J. C. Jung, E. L. Cheung, and M. J. Schnitzer, "Fiber-optic fluorescence imaging," Nat. Methods **2**(12), 941–950 (2005).
2. K. Carlson, M. Chidley, K. B. Sung, M. Descour, A. Gillenwater, M. Follen, and R. Richards-Kortum, "In vivo fiber-optic confocal reflectance microscope with an injection-molded plastic miniature objective lens," Appl. Opt. **44**(10), 1792–1797 (2005).
3. A. R. Rouse and A. F. Gmitro, "Multispectral imaging with a confocal microendoscope," Opt. Lett. **25**(23), 1708–1710 (2000).
4. W. Göbel, J. N. D. Kerr, A. Nimmerjahn, and F. Helmchen, "Miniaturized two-photon microscope based on a flexible coherent fiber bundle and a gradient-index lens objective," Opt. Lett. **29**(21), 2521–2523 (2004).
5. V. Szabo, C. Ventalon, V. De Sars, J. Bradley, and V. Emiliani, "Spatially selective holographic photoactivation and functional fluorescence imaging in freely behaving mice with a fiberscope," Neuron **84**(6), 1157–1169 (2014).
6. P. Alter, C. Bayrouty, J. Benoit, and R. Zacek, *An Introduction to Fiber Optic Imaging* (SCHOTT North America, 2007), 2nd edition.
7. N. Tabatabaei, D. Kang, M. Kim, T. Wu, C. N. Grant, M. Rosenberg, N. S. Nishioka, P. E. Hesterberg, J. Garber, Q. Yuan, A. J. Katz, and G. J. Tearney, "Clinical Translation of Tethered Confocal Microscopy Capsule for Unsedated Diagnosis of Eosinophilic Esophagitis," Sci. Rep. **8**(1), 2631 (2018).
8. O. Homburg, D. Hauschild, and V. Lissotschenko, "Manufacturing and Application of Micro□Optics: An Enabling Technology for the 21st Century," Optik Photonik **3**(4), 48–52 (2008).
9. J. C. Jung, A. D. Mehta, E. Aksay, R. Stepnoski, and M. J. Schnitzer, "In vivo mammalian brain imaging using one- and two-photon fluorescence microendoscopy," J. Neurophysiol. **92**(5), 3121–3133 (2004).
10. G. Oh, E. Chung, and S. H. Yun, "Optical fibers for high-resolution in vivo microendoscopic fluorescence imaging," Opt. Fiber Technol. **19**(6), 760–771 (2013).
11. R. P. Barretto, B. Messerschmidt, and M. J. Schnitzer, "In vivo fluorescence imaging with high-resolution microlenses," Nat. Methods **6**(7), 511–512 (2009).
12. J. C. Jung and M. J. Schnitzer, "Multiphoton endoscopy," Opt. Lett. **28**(11), 902–904 (2003).
13. G. Meng, Y. Liang, S. Sarsfield, W. C. Jiang, R. Lu, J. T. Dudman, Y. Aponte, and N. Ji, "High-throughput synapse-resolving two-photon fluorescence microendoscopy for deep-brain volumetric imaging in vivo," eLife **8**, e40805 (2019).
14. M. E. Bocarsly, W. C. Jiang, C. Wang, J. T. Dudman, N. Ji, and Y. Aponte, "Minimally invasive microendoscopy system for in vivo functional imaging of deep nuclei in the mouse brain," Biomed. Opt. Express **6**(11), 4546–4556 (2015).
15. X. D. Li, S. A. Boppart, J. Van Dam, H. Mashimo, M. Mutinga, W. Drexler, M. Klein, C. Pitris, M. L. Krinsky, M. E. Brezinski, and J. G. Fujimoto, "Optical coherence tomography: advanced technology for the endoscopic imaging of Barrett's esophagus," Endoscopy **32**(12), 921–930 (2000).
16. J. G. Fujimoto, "Optical coherence tomography for ultrahigh resolution in vivo imaging," Nat. Biotechnol. **21**(11), 1361–1367 (2003).
17. D. J. Cai, D. Aharoni, T. Shuman, J. Shobe, J. Biane, W. Song, B. Wei, M. Veshkini, M. La-Vu, J. Lou, S. E. Flores, I. Kim, Y. Sano, M. Zhou, K. Baumgaertel, A. Lavi, M. Kamata, M. Tuszynski, M. Mayford, P. Golshani, and A. J. Silva, "A shared neural ensemble links distinct contextual memories encoded close in time," Nature **534**(7605), 115–118 (2016).
18. S. L. Resendez, J. H. Jennings, R. L. Ung, V. M. Namboodiri, Z. C. Zhou, J. M. Otis, H. Nomura, J. A. McHenry, O. Kosyk, and G. D. Stuber, "Visualization of cortical, subcortical and deep brain neural circuit dynamics during naturalistic mammalian behavior with head-mounted microscopes and chronically implanted lenses," Nat. Protoc. **11**(3), 566–597 (2016).
19. S. Ohmi, H. Sakai, Y. Asahara, S. Nakayama, Y. Yoneda, and T. Izumitani, "Gradient-index rod lens made by a double ion-exchange process," Appl. Opt. **27**(3), 496–499 (1988).
20. M. A. Tadayon, I. Pavlova, K. M. Martyniuk, A. Mohanty, S. P. Roberts, F. Barbosa, C. A. Denny, and M. Lipson, "Microphotonic needle for minimally invasive endoscopic imaging with sub-cellular resolution," Sci. Rep. **8**(1), 10756 (2018).
21. T. Gissibl, S. Thiele, A. Herkommer, and H. Giessen, "Two-photon direct laser writing of ultracompact multi-lens objectives," Nat. Photonics **10**(8), 554–560 (2016).
22. T. Gissibl, S. Thiele, A. Herkommer, and H. Giessen, "Sub-micrometre accurate free-form optics by three-dimensional printing on single-mode fibres," Nat. Commun. **7**(1), 11763 (2016).
23. S. Thiele, K. Arzenbacher, T. Gissibl, H. Giessen, and A. M. Herkommer, "3D-printed eagle eye: Compound microlens system for foveated imaging," Sci. Adv. **3**(2), e1602655 (2017).
24. P.-I. Dietrich, M. Blaicher, I. Reuter, M. Billah, T. Hoose, A. Hofmann, C. Caer, R. Dangel, B. Offrein, U. Troppenz, M. Moehrle, W. Freude, and C. Koos, "In situ 3D nanoprinting of free-form coupling elements for hybrid photonic integration," Nat. Photonics **12**(4), 241 (2018).

Optics EXPRESS


25. A. Giovannucci, A. Badura, B. Deverett, F. Najafi, T. D. Pereira, Z. Gao, I. Ozden, A. D. Kloth, E. Pnevmatikakis, L. Paninski, C. I. De Zeeuw, J. F. Medina, and S. S. Wang, "Cerebellar granule cells acquire a widespread predictive feedback signal during motor learning," Nat. Neurosci. **20**(5), 727–734 (2017).
26. K. K. Ghosh, L. D. Burns, E. D. Cocker, A. Nimmerjahn, Y. Ziv, A. E. Gamal, and M. J. Schnitzer, "Miniaturized integration of a fluorescence microscope," Nat. Methods **8**(10), 871–878 (2011).
27. C. A. Denny, M. A. Kheirbek, E. L. Alba, K. F. Tanaka, R. A. Brachman, K. B. Laughman, N. K. Tomm, G. F. Turi, A. Losonczy, and R. Hen, "Hippocampal memory traces are differentially modulated by experience, time, and adult neurogenesis," Neuron **83**(1), 189–201 (2014).
28. L. Madisen, T. Mao, H. Koch, J. M. Zhuo, A. Berenyi, S. Fujisawa, Y. W. Hsu, A. J. Garcia 3rd, X. Gu, S. Zanella, J. Kidney, H. Gu, Y. Mao, B. M. Hooks, E. S. Boyden, G. Buzsáki, J. M. Ramirez, A. R. Jones, K. Svoboda, X. Han, E. E. Turner, and H. Zeng, "A toolbox of Cre-dependent optogenetic transgenic mice for light-induced activation and silencing," Nat. Neurosci. **15**(5), 793–802 (2012).
29. R. Fain, F. Barbosa, J. Cardenas, and M. Lipson, "Photonic Needles for Light Delivery in Deep Tissue-like Media," Sci. Rep. **7**(1), 5627 (2017).
30. A. A. Sharp, A. M. Ortega, D. Restrepo, D. Curran-Everett, and K. Gall, "In vivo penetration mechanics and mechanical properties of mouse brain tissue at micrometer scales," IEEE Trans. Biomed. Eng. **56**(1), 45–53 (2009).
31. M. A. Tadayon, Q. Li, A. Mohanty, and M. Lipson, "Integrated nanophotonic platform for high bandwidth and high resolution optogenetic excitation," in CLEO: Applications and Technology (Optical Society of America, 2016), pp. ATu4O-4.
32. J. W. Goodman, *Introduction to Fourier Optics* (Roberts and Company Publishers, 2005).